Insulin Dimer Dissociation and Unfolding Revealed by Amide I Two-Dimensional Infrared Spectroscopy

Insulin Dimer Dissociation and Unfolding Revealed by Amide I Two-Dimensional Infrared Spectroscopy

Ziad Ganim,[a] Kevin C. Jones[a] and Andrei Tokmakoff[a]*

Received (in XXX, XXX) Xth XXXXXXXXX 200X, Accepted Xth XXXXXXXXX 200X
First published on the web Xth XXXXXXXXX 200X
DOI: 10.1039/b000000x

The monomer-dimer transition of insulin has been probed with two-dimensional infrared spectroscopy and related infrared spectroscopies to isolate spectral signatures of the conformational changes concomitant with dissociation. These experiments were atomistically interpreted using 2D IR spectra calculated from an ensemble of monomer and dimer structures including the effects of disorder, which provided a complement and a point of comparison to NMR and x-ray crystallography models. The amide I $\nu_{\perp}$ mode, which is delocalized over both monomer units through an intermolecular antiparallel β sheet, was lost upon dimer dissociation and shifts were observed in the $\nu_{\parallel}$ β-sheet and α-helix bands. These spectral changes provided a structurally sensitive probe of dimer dissociation, which was used to measure the binding constant, K_D, and to parameterize a thermodynamic model for the dimer fraction. The solvent conditions surveyed the effects of ethanol and salt addition on the dimer fraction in acidic, deuterated water as a function of temperature. It was found that addition of ethanol had a significant destabilizing effect on the dimer state, and shifted K_D from 70 μM in D_2O to 7.0 mM in 20% EtOD at 22 °C. Simulation of the monomer 2D IR spectra indicates that the B-chain C terminus is partially disordered, although not fully solvated by water.

1. Introduction

Insulin homodimerization is one of the simplest protein-protein binding reactions involving a secondary structural change. Insulin is a 51 amino acid, mostly α-helical protein that dimerizes through the formation of an intermolecular β sheet[1]. It is known that the binding region becomes disordered or partially unfolded when dissociated into its monomeric state.[2,3,4,5,6,7,8,9] Although questions concerning the monomer structure and degree of disorder remain, the fact that dimer is more ordered than monomer raises fundamental questions about coupled folding and binding processes, and stands in contrast to classical rigid-body association models.[10,11] How do two partially disordered proteins encounter one another, locate specific intermolecule contacts, and fold? Despite the volume of research on insulin, there have been no postulated mechanisms for how folding and association couple in the dimerization of insulin.

Inspection of the dimer crystal structure[1] (**Fig. 1**a) shows that insulin has a network of hydrophobic contacts that spans across both monomer units and stabilizes the dimer (**Fig. 1**b). When ordered, the dimer interface is largely flat, and is comprised of aromatic and aliphatic residues. The packing of these nonpolar sidechains is reinforced and given specificity by backbone hydrogen bonds between C-terminal residues on the B chains. The B chain holds a critical set of contacts for dimer formation and the degree to which it is folded determines how much ordering is required to form the dimer. Models for the monomer (**Fig. 1**c and 1d)[2,3,4,5,6,7,8,9] have provided conflicting evidence on whether the B chain is extended into the solvent or if it resembles its conformation in the dimer. An extended conformation of the B chain would expand the radius of gyration for the protein and allow it to make weak, non-specific contacts. This scenario is consistent with the fly-casting mechanism for reducing the entropic cost for a binding transition state.[12] Alternatively, if the B chain largely resembles its conformation in the dimer, insulin monomers may dimerize by making native contacts with largely ordered interfaces. Thus, placing a collection of experimental constraints on the monomer structure may help suggest important reaction coordinates for describing protein association.

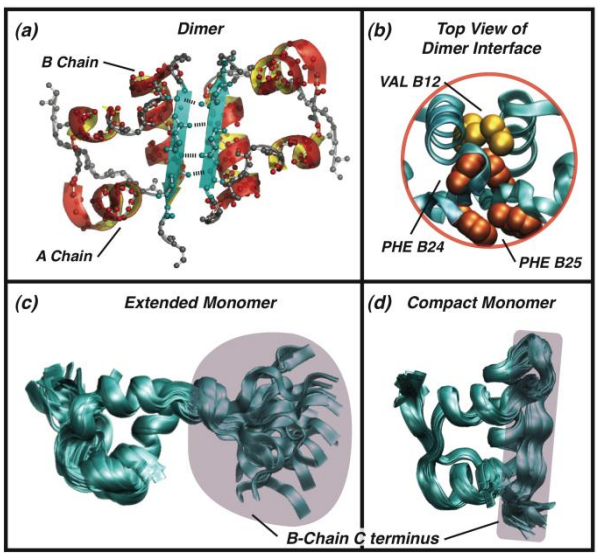

Fig. 1 Structural visualizations of insulin dimer and monomer models from PDB IDs 4INS (a,b), 1JCO (c), and 2JV1 (d). Structures visualized using VMD[81] and POV-Ray.[83]

The methods used to study the monomer-dimer equilibrium of insulin have typically focused either on structure or association state, however sensitivity to both is required for an ideal probe of binding and folding. Assays that have used sedimentation,[13,14,15] scattering,[16] kinetics,[17] mass spectrometry,[18] ultraviolet absorption,[19] fluorescence depolarization,[20,21], pulsed field-gradient spin-echo NMR[22] and FRET[23] provide sensitivity to the monomer/dimer ratio and may be used to quantify the dissociation constant, K_D, but they lack secondary structural sensitivity. Circular dichroism[24,25] has been deconvoluted to yield a mix of qualitative structural resolution and sensitivity to the association state. Infrared vibrational spectroscopy has been used to study insulin fibrilization,[26,27] but it has not revealed any changes about the monomer/dimer transition. Since the insulin dimer forms the asymmetric unit, X-ray crystallography has provided atomistic structures for various polymorphs of the insulin dimer and hexamer,[1,28,29] but has not yielded a native monomer structure. Nuclear magnetic resonance (NMR) spectroscopy has yielded the most information about insulin in solution via a series of hexamer,[30,31] and dimer[32,33] structures. Due to the poor sensitivity of NMR at micromolar concentrations, many investigations of the insulin monomer have relied on mutants or co-solvent addition;[2,3,34,4,7,8,32,35] while the resulting set of structures have generated growing agreement that insulin is more disordered in the monomer state than in the dimer, there has been no quantitative-level agreement. Moreover, neither crystallography nor 2D NMR have yielded a measurement of K_D.

Amide I two-dimensional infrared spectroscopy (2D IR) provides a number of advantages for studying conformational dynamics of proteins. 2D IR probes the intrinsic vibrations of a protein that are seen in FTIR spectra, but with enhanced resolution due to an additional frequency dimension. This allows for the correlation of absorption and emission frequencies to yield diagnostic 2D lineshapes and cross-peaks. When probing the amide I band, 2D IR provides distinct signatures for anti-parallel β sheets that report on their size and symmetry.[36] Signature lineshapes are also observed for α helices, which may overlap with the vibrations of disordered regions. Because amide I peaks arise from delocalized vibrations, they report on the structural relationships among secondary structural motifs. Moreover, the methodology exists to calculate 2D IR spectra from molecular dynamics simulations.[37,38,39,40] This can be used to extract structures from 2D IR spectra through an iterative process of structure refinement and spectral calculations. In addition, the structure-based modeling can be used to interpret the spectra[41,42,43] and provide an atomistic description of the vibrational modes being probed. Amide I 2D IR spectra, applications, and modeling have been the topic of recent reviews.[37,44,38,45,46,46]

In this manuscript, 2D IR spectroscopy and simulations are used to develop insulin dimer dissociation as a model system for investigations of the biophysics of coupled protein folding/binding. The amide I monomer and dimer signatures are experimentally determined using various types of 2D IR spectroscopy. Fitting of these signatures was used to quantify the dissociation constant and parameterize a two-state model for the thermodynamics. The spectral signatures are interpreted in atomistic detail using structure-based modeling; 2D IR spectra were calculated using molecular dynamics simulations of insulin drawing on crystal structure and solution NMR models.

2. Methods

2.1 Sample preparation

Insulin from bovine pancreas was obtained from Sigma-Aldrich (St. Louis, MO) and used in all of the experiments described in this manuscript. The sample was H/D exchanged for infrared studies by twice dissolving it in D_2O at ~1 mg/mL, heating to 60 °C for 1 h, and lyophilizing it. Full H/D exchange was verified by the loss of the protonated amide II band at 1550 cm^{-1}. All of the buffers used were based on 0.27 M DCl in D_2O and some buffers included EtOD. All of the deuterated reagents were obtained from Cambridge Isotope Laboratories, Inc. (Andover, MA), and verified to be zinc free to further inhibit the formation of aggregates.

2.2 2D IR Experiments

The 2D IR spectra were acquired using IR pulses that were resonant with the amide I band at ~1660 cm^{-1}, using methods that have been described elsewhere.[47,42,48] The FWHM bandwidths were 90 fs in time and 165 cm^{-1} in energy as measured by TG FROG. Four types of nonlinear spectra are reported in this manuscript: 2DIR absorptive spectra, NRPS, RPS and HDVE. The absorptive 2D IR correlation spectrum, which is the sum of rephasing and nonrephasing spectra, was the principal tool because it yields the highest resolution features. The coherence times (τ_1) for rephasing and non-rephasing experiments were scanned in 4 fs steps to 4 ps and 2.5 ps, respectively. The waiting time, τ_2, was zero in all spectra. The power spectra of the rephasing (RPS) and nonrephasing (NRPS) contributions were also analyzed independently because their interference patterns tend to highlight diagonal and off-diagonal features, respectively. Heterodyne-detected dispersed vibrational echo spectra (HDVE) are the ω_3-axis projection of the 2D IR correlation spectrum, and can be rapidly obtained without scanning any time delays.[48] In this manuscript, only the phase-insensitive HDVE power spectra were used. HDVE spectra were acquired using the FTSI method[48] under conditions identical to the 2D IR spectra, except τ_1 was fixed at 0 fs, and τ_{LO} was set to 4 ps. The relative polarization between the first two excitation pulses and the third/LO determined whether the collected spectra were for parallel (ZZZZ) or pependicular (ZZYY) conditions. Further experimental details and an explanation of how spectra containing insulin aggregates were rejected (due to a signature 1615 cm^{-1} peak) are provided in the Supporting Information.

The samples were held in a home-built brass cell equipped with 1 mm thick CaF_2 windows and a 50 μm Teflon spacer. The temperature was controlled by coupling the brass sample cell to a recirculating water bath. Infrared absorption spectra

were acquired in a Nicolet 380 FT IR spectrometer using the same sample cell.

2.3 Simulations: MD, Calculating Spectra, and Bright State Analysis

To help interpret the experiments, 2D IR spectra were calculated for three structural models derived from the porcine insulin dimer (PDB ID: 4INS)[1], the human insulin monomer in 35% CD_3CN (PDB ID: 2JV1)[7], and an engineered, monomeric human insulin mutant (PDB ID: 1JCO)[4]. All of the structures were simulated in GROMACS 3.3.1.[49,50,51,52,53,54,55] In the simulation procedure, missing protons were filled in, and the structures were energy-minimized for up to 10000 steps to conform to the OPLS/AA[56,57,58,59,60,61,62] force field parameters. The protein structures were solvated[63] with SPC/E water[64] and position-constrained during 100 ps of dynamics in the NPT ensemble at 300 K and 1 atm. After all of these equilibration steps, molecular dynamics were run in the same NPT ensemble, and structures of the entire solvent box were saved each 20 fs for calculating IR spectra. The dimer was simulated for 1 ns and each structure of the monomer ensembles (2JV1 has 50 structures and 1JCO has 25 structures) was simulated for 100 ps.

The IR absorption spectra and 2D IR spectra were calculated using the previously described code,[37] which has been upgraded to incorporate developments in the models.[65,66,67] The 2D IR spectra were calculated using site energies derived from the electrostatic potential across each amide unit[68] and a combination of electrostatic and DFT-derived coupling between sites.[65] To better approximate the dynamics, the time-averaging approximation[67,66] was used with a Gaussian window of 170 fs. Since the dimer contained 98 sites, a new block diagonalization procedure was employed to make the two-quantum matrix diagonalizations more computationally efficient. Coupling values less than 4 cm^{-1} in magnitude are set to zero only if they lead to the formation of a new block, and further details are described in the Supplementary Information. All of the simulated frequencies are corrected for systematic errors with a 20 cm^{-1} redshift.

The vibrational wavefunctions were visualized using a doorway mode analysis of the simulated spectra, as described previously[69,70,71]. The bright states that characterize the influence of particular amide I vibrations on the infrared spectrum were calculated from the eigenstates of the entire trajectory corresponding to energies within a frequency window. To calculate the mode decomposition, bright states were calculated for a 5 cm^{-1} sliding window across the spectrum. Then, each bright state was decomposed into contributions from the residues in chosen motifs (α helices, β sheets, and unstructured regions) by summing the squared amplitudes for residues in each respective structural motif. In the ideal scenario, the amplitude of the first bright state dominates the total. For all of the calculations in this manuscript, the first bright state was the only one considered, and this was found to carry 0.41-0.44 of the total intensity, with no dependence on frequency or structure.

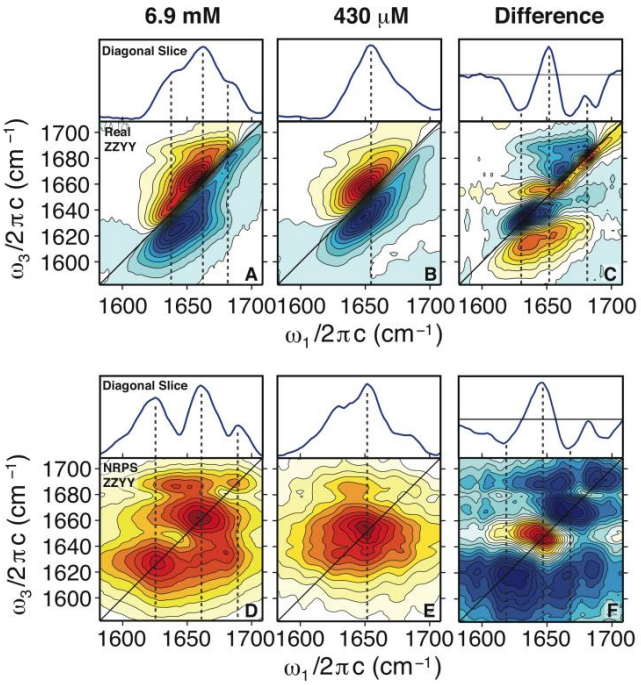

Fig. 2 Concentration-dependent ZZYY 2D IR spectra and difference spectra acquired in 0.27 M DCl 20% (v/v) EtOD:D_2O. (top) Absorptive spectra; (bottom) NRPS. All contours are plotted in 8.3% intervals. Slices along the diagonal ($\omega_1 = \omega_3$) are plotted above each spectrum, except for panel A and B, where the slices chosen to coincide with the peak maximum ($\omega_1+\Delta = \omega_3$).

3. Results

3.1 Concentration-Dependent 2D IR Spectral Features

To reveal the secondary structural changes associated with insulin dimerization, concentration-dependent 2D IR spectra were acquired in 20% ethanol. Figure 2 shows the absorptive and NRPS representations under for monomeric conditions (430 μM) and at higher concentrations where dimer fraction is ~50% (6.9 mM). The dimer spectra are consistent with previously observed spectra of mixed α/β proteins, which show a Z-shaped contour lineshape, indicative of a β sheet. (To interpret basic features of 2D IR spectra, the reader is referred to Ref. 46).

In each of the dimer 2D IR spectra (Fig. 2A and 2D), three peaks can be seen along the diagonal, which are highlighted in the diagonal slices plotted above each spectrum. Focusing on the absorptive ZZYY spectra, the most intense peak appears at ω_1 = 1657 cm^{-1}, and can be attributed to α-helical vibrations based on empirical assignments. The second most intense peak at 1645 cm^{-1} corresponds to $\nu_\perp$ vibrations of the β sheet, named by the fact that its transition dipole lies perpendicular to the strands of the β-sheet. At 1690 cm^{-1} there is a peak corresponding to its inverted symmetry partner, the $\nu_{||}$ β-sheet mode, which may also include contributions from β turns. The same vibrations are observed in the NRPS as distinct peaks due to the interference effects inherent to non-rephasing spectra, and are broader due to the inclusion of imaginary contributions to power spectra.

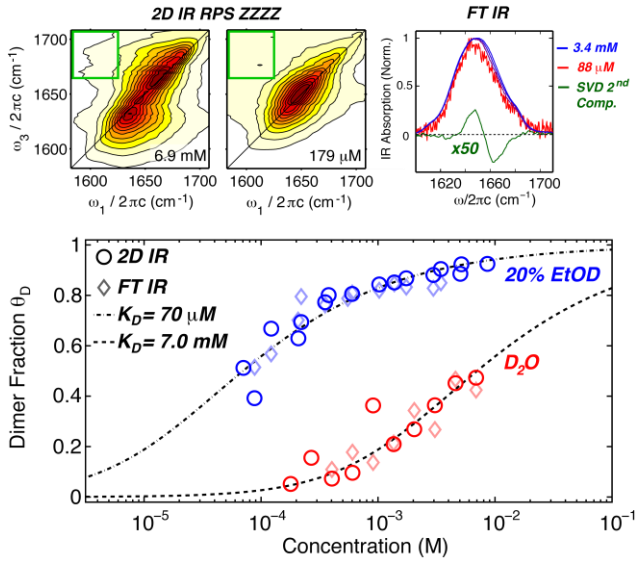

Fig. 3 Extraction of dimer fraction from FTIR and 2D IR rephasing power pectra (RPS). Representative RPS spectra, and the FTIR series and 2nd SVD component are shown on top. Concentration-normalized off-diagonal integration of 2D IR spectra and second component SVD amplitudes of FTIR spectra were fit to the dimer fraction (eqs. 1-2) to extract K_D (bottom).

among the α-helical and β-sheet vibrations, which are most easily distinguished in the NRPS (Fig 2D). A cross peak between the two β-sheet vibrations is observed along the horizontal corresponding to ω_3=1635 cm^{-1} and cross peaks between $\nu_{||}$ and both $\nu_{\perp}$ and the α-helical mode appear at ω_1 and ω_3 = 1690 cm^{-1}. The linewidth of these peaks gives rise to cross-peak ridges, or broadening along the ω_1 dimension. This effect is enhanced in the absorptive 2D IR spectra.

The monomer 2D IR spectra (Fig. 2B and 2E) show one clear peak that is similar to the α-helical feature in the dimer spectra, but it is downshifted to 1650 cm^{-1}. At predominantly monomer concentrations, the $\nu_{\perp}$ mode and its cross-peaks are greatly suppressed, although weak features arising from the β-sheet modes remain. Inspection of the NRPS diagonal slice shows that the higher frequency, 1690 cm^{-1} peak still appears in the monomer spectra. The difference spectra (Fig. 2C and 2F) summarize the spectral changes that occur as the equilibrium is shifted towards insulin monomers; there is a diagonal narrowing of the spectrum due to the loss of intensity at 1635 cm^{-1} and 1690 cm^{-1} in the diagonal and cross-peak regions, and the peak maximum shifts from 1665 to 1650 cm^{-1}

3.2 K_D Measurements

To provide further evidence that the spectral changes arise from dimer dissociation and to insure consistency with previous investigations, concentration-dependent FTIR and ZZZZ 2D IR spectra were acquired in the range of 88 μM to 6.9 mM in D_2O and 400 μM to 6.9 mM in 20% EtOD:D_2O. Since spectral intensities in both experiments are linear in concentration, changes in concentration-normalized spectra will reflect monomer or dimer fraction. Under these conditions the integrated area in FTIR spectra remained constant, indicating no significant change in transition dipole moments between the monomer and dimer states.

Fig. 3 shows the analysis of FTIR and 2D IR RPS to obtain the dissociation constant, K_D. Across the concentration range, the changes to the FTIR spectra are barely discernible. The spectra can be described without *a priori* knowledge of the monomer and dimer spectra by singular value decomposition (SVD) analysis, which reveals a slight red shift with concentration. The dimer population was obtained from 2D IR by integrating the off-diagonal region of the RPS that included β-sheet signatures from the dimer (ω_1 = 1582–1624 cm^{-1}, ω_3 = 1664–1708 cm^{-1}). This region, illustrated in Fig. 3, was chosen for its large monomer/dimer contrast, insensitivity to phasing and non-resonant contributions, and favorable signal-to-noise. The concentration-normalized 2D IR intensities and FTIR second component SVD amplitudes, $I(c)$, were taken to be proportional to the dimer fraction,

$$aI(c)+b=\theta_D(c) \qquad \text{Eq. 1}$$

$$\theta_D(c)=\frac{4c+K_D-\sqrt{K_D^{\,2}+8K_Dc}}{4c}. \qquad \text{Eq. 2}$$

Here c is the total insulin concentration, and a, b, and K_D were the fit parameters. K_D values of 70 μM and 55 μM were extracted from the 2D IR and FTIR measurements in D_2O, respectively. Addition of 20% ethanol shifted K_D to 7.0 mM and 6.0 mM according to 2D IR and FTIR fits. In D_2O, this K_D is consistent with the previously observed values in protonated solvents at similar pHs and ionic strengths, which range from 25 μM to 261 μM. Although the destabilizing effect of ethanol on insulin dimers has been observed,[72,20] these data show the first corresponding K_D measurement.

3.3 Temperature-Dependent 2D IR Spectral Features

Temperature can also be used to control the monomer/dimer equilibrium of insulin. Fig 4. shows temperature-dependent 2D IR spectra collected at 1.7 mM. At 20°C, the 2D IR spectrum has a single clear peak at 1655 cm^{-1} with high and low frequency shoulders at 1637 cm^{-1} and 1676 cm^{-1}, which are similar to the features associated with increasing dimer content in Fig. 2A. Moreover, a similar pattern of cross-peak ridges is observed among the β-sheet and α-helix vibrations, most clearly visible at ω_3=1680 and 1620 cm^{-1}. The difference spectra show the loss of distinct peaks along the diagonal and in the cross-peak regions; the loss of both positive and negative lobes of the cross-peak between the $\nu_{\perp}$ and $\nu_{||}$ modes can be seen at ω_1~1680 cm^{-1}. In addition to the temperature-dependent changes induced by dimer dissociation, the 2D IR spectra will reflect thermal changes to the vibrational

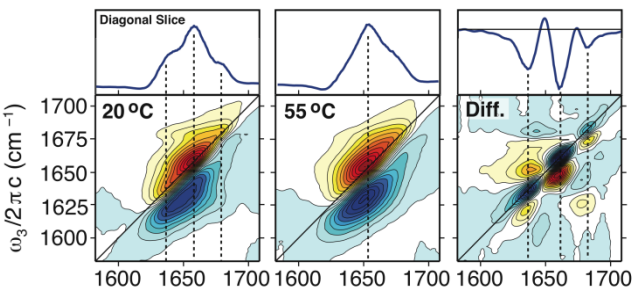

Fig. 4 ZZYY spectra were acquired for 1.7 mM insulin concentration in 0.27 M DCl, 0.1 M NaCl 20% EtOD:D_2O. All spectra show contours plotted in 8.3% intervals.

dynamics and increased solvent transmission. However, the similarity between the dimer and monomer signatures between the temperature- and concentration-dependent 2D IR spectra provides conclusive evidence that increasing the temperature induces dimer dissociation.

3.4 Solvent-Dependent Thermal Dissociation and Unfolding

For a more extensive characterization of the insulin binding thermodynamics, the temperature dependence of dimer dissociation was quantified in eleven different solvent conditions using HDVE. Because the HDVE spectrum is formally equivalent to an ω_3 projection of the 2D IR spectrum, its power spectra are a phase-insensitive measurement that retain vibrational coupling information, and can be acquired rapidly without scanning any time-delays. The set of solvents was chosen to test the effects of adding ethanol and sodium chloride salt to the thermal dissociation at 1.7 mM (10 mg/ml). Fig. 5A shows representative HDVE thermal dissociation data in 0.27 M DCl 30% EtOD:D_2O. The salient changes to the HDVE spectrum are a narrowing with temperature due to a shift of intensity from 1640 and 1690 cm^{-1} to 1650 cm^{-1}, which is consistent with the 2D IR changes seen in Fig. 4. The addition of salt had less of an effect on the thermal dissociation than ethanol, and its effects were not additive with ethanol (See Supplementary Information, Fig. 11).

The temperature-dependent HDVE spectra in all ethanol-containing solvents were decomposed into a two-state basis derived using SVD analysis on the data set in 0.27 M DCl, 0.1 M NaCl 20% (v/v) EtOD:D_2O. Use of the same basis spectra allowed for a faithful comparison of the temperature-dependence across the solvent conditions. The melting curves in Fig. 5C show that increasing the ethanol concentration dropped the melting temperature by roughly 3.5°C for each 10% addition of ethanol and reduced aggregation. When the ethanol content was less than 20%, aggregation was a limiting factor for acquiring spectra at temperatures >50°C. Cold-induced aggregation was also seen that may be a sign of cold-induced dissociation, which is predicted by the two-state thermodynamics. One key feature of 2D IR spectroscopy is that the transition dipole scaling makes the distinct 1615 cm^{-1} mode of β-sheet aggregates appear intensely, which allows these spectra to be excluded from the analysis. (See Supplementary Information for details). The fits were performed over temperatures that were aggregation-free for all samples. An identical analysis was performed on the experiments with salt-containing solvents, although more emphasis will be placed on the ethanol results due to their reduction of aggregation.

3.5 Thermodynamic Modeling

After decomposing the spectra into a basis derived from SVD analysis, the second component amplitudes were fit using a thermodynamic model that extended two-state models for protein unfolding[73] with concentration dependence,

$$D \rightleftharpoons 2M \qquad \text{Eq. 3}$$

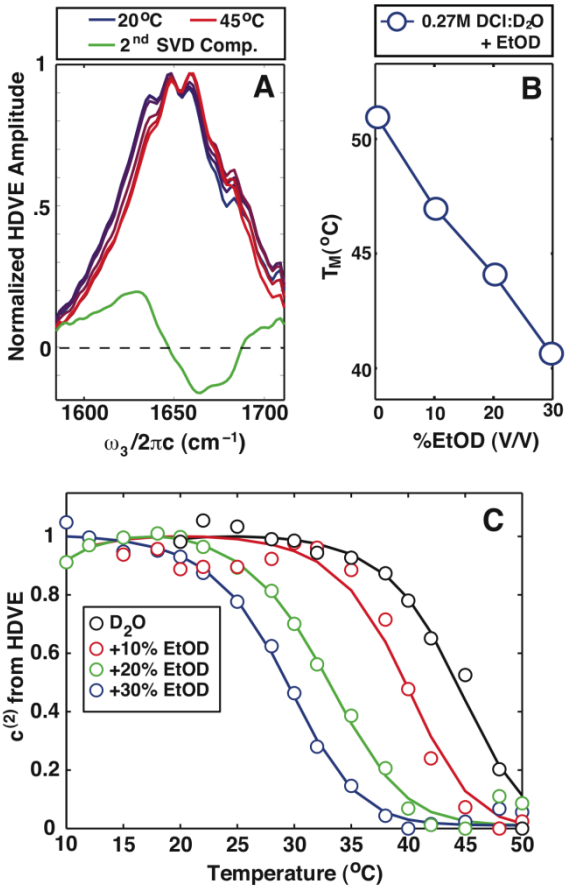

Fig. 5 Temperature-dependent HDVE spectra were acquired as a function of ethanol co-solvent concentration. Spectra were acquired in 2.5 °C intervals from 10 - 55 °C. Representative spectra and 2nd SVD component are shown in panel A for 30% EtOD. Extracted melting temperatures and amplitudes of the second SVD are shown in B and C.

$$\Delta G = \Delta H^0 - T\Delta S^0 + \Delta C_P\left[T - T_M - T\ln(T/T_M)\right] \qquad \text{Eq. 4}$$

$$\Delta G = -RT\ln\frac{{c_M}^2}{c_D} \qquad \text{Eq. 4}$$

where ΔG, ΔH^0, ΔS^0, and ΔC_P are the free energy, enthalpy, entropy, and heat capacity changes, and T_M is defined as ΔG=0, which may not be where the normalized melting curves intercept ½. The second component amplitude was assumed to be proportional to the dimer fraction defined as

$$\theta_D(T) = \frac{2c_D}{2c_D + c_M}, \qquad \text{Eq. 5}$$

where c_M and c_D are the concentrations of monomers and dimers. To fit the thermal dissociation curves, T_M, ΔH^0, and ΔC_P were varied and the resulting K_D was used to calculate θ_D(T) using the standard state of c_0=1 M such that ΔG=0 if K_D=1 M. These fits were constrained by our measurement of the equilibrium constants at 22 °C and considered data at temperatures that were aggregation-free. The equilibrium constant measured in 20% ethanol was assumed to be representative of solvents with 10-30% ethanol. For the reference solvent of 1.7 mM insulin in 0.27 M DCl:D_2O, the extracted parameters were T_M=51 °C, ΔH^0=135 kcal/mol and

ΔC_P=5 kcal/mol K. At 22 °C, ΔH = -9.6 kcal/mol, ΔS = 51 cal/mol K and ΔG = 5.4 kcal/mol. (Full details of the solvent-dependent changes to the melting curves are present in the Supplementary Material.) Upon addition of 30% ethanol, T_M dropped by 11 °C, $\Delta\Delta H^0$ was -60 kcal/mol and $\Delta\Delta C_P$ was -2 kcal/mol K, which indicated greatly reduced stability of the dimer state relative to the monomer. The addition of 100 mM salt caused minor changes relative to ethanol addition; it reduced T_M by 5 °C in the reference solvent and increased T_M by 1.5 °C when added to 20% ethanol conditions. In summary, ethanol was found to be an effective co-solvent for destabilizing the insulin dimer state relative to the monomer without any significant changes to the spectral features (See Supplementary Information, Fig. 8).

3.6 Structural modeling of insulin 2D IR spectra

A key feature of amide I protein 2D IR spectra is the ability to make atomistic assignments with structure-based modeling. To interpret the 2D IR spectra, MD simulations were performed on structural models obtained from x-ray crystallography or solution NMR spectroscopy and the spectra appear in Fig. 6. Since the spectra in the amide I region arise almost entirely from backbone vibrations, models for different insulin secondary structures can be compared, even in cases such as these where the primary structure displays minor variation from the experiment. The 2D IR spectra calculated from static structure snapshots in the trajectory displayed fine structure from many peaks. Each structure was solvated and dynamics were run to sample the small-amplitude, sub-ns solvent and protein fluctuations (10,000 – 50,000 frames) to obtain smooth lineshapes consistent with the experiments.

The calculated 2D IR correlation spectrum for the dimer shows three diagonal features: two well-defined peaks at ω_1 = 1634 and 1660 cm^{-1} and a shoulder at 1678 cm^{-1}, which nominally correspond to the $\nu_\perp$ β-sheet mode, α-helical modes, and the $\nu_{||}$ β-sheet modes assigned for the dimer spectrum in Fig. 6A (all calculated frequencies are corrected with a systematic ~20 cm^{-1} redshift). While it is a subtle feature in the calculated spectra, the high-frequency shoulder is further evidenced by the cross-peak ridge extending horizontally from the diagonal at 1678 cm^{-1}. The positions of the $\nu_\perp$ and α-helix bands match the experiment exactly, but the $\nu_{||}$ mode is 10 cm^{-1} too red-shifted. Another difference with respect to the experiment is that the intensity of the α-helix peak is ~50% too low in the calculation relative to the β-sheet modes. These difference may be due to the structural differences between the solution and crystalline dimer states or errors in the calculation. Examination of the corresponding NRPS shows discrete cross-peaks between $\alpha/\nu_{||}$ modes at (1655/1676 cm^{-1}) and $\nu_{||}/\nu_\perp$ modes at (1675/1627 cm^{-1}), with a similar overall structure to the experimental NRPS.

There are varying proposals for the structure of the insulin monomer, which differ in the conformation of the B chain C-terminus that folds and stabilizes dimer contacts. 2D IR spectra have been calculated based on two ensembles resulting from solution NMR experiments (**Fig. 1**). These structures place a lower limit on the amount of disorder that may be observed in 2D IR spectra, due to the fact that the ns-μs

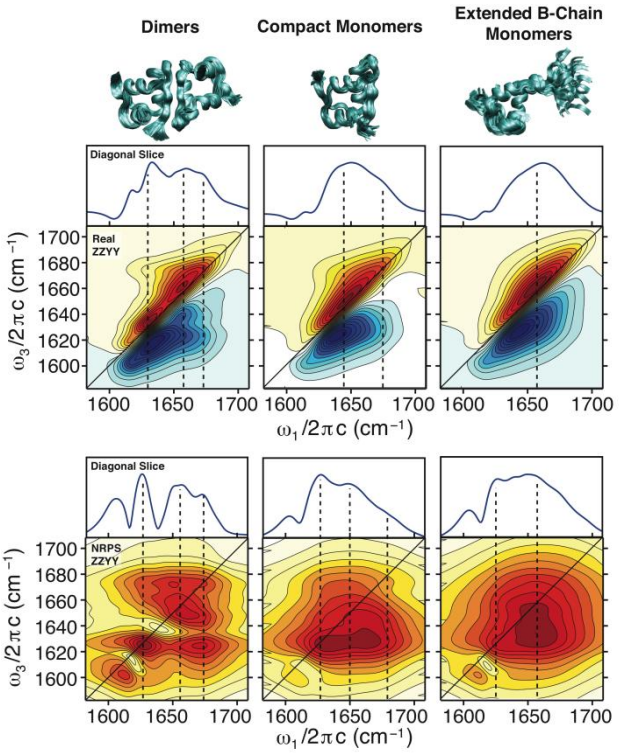

Fig. 6 Simulated 2D IR spectra for dimers (4INS), compact monomers (1JCO) and extended B-chain monomers (2JV1). The intensity at 1620 cm^{-1} includes an exaggerated contribution from proline. Structures visualized using VMD[81] and POV-Ray.[83]

fluctuations of the B chain terminus would be in the partial-complete motionally narrowed limit for 30-200 ms mixing time NMR experiments, but in the static limit for 2D IR experiments with 4 ps coherence times. (Evidence for poor separation of these timescales has been observed in the anomalous variation of amide line widths in insulin.[74]) One of the monomer ensembles was comprised of 50 compact structures with B chains that strongly resembled the conformation in the dimer (PDB ID: 2JV1). The second ensemble (PDB ID: 1JCO) contained 26 structures with extended B chain C termini, and more disorder in the N-terminal B-chain region and the A-chain helices. The resulting spectra were summed over the respective ensembles and the results appear in Fig. 6. Each of the calculated monomer spectra shows features that resemble the experimental monomer spectra (Fig. 2B and 2E), but neither one entirely reproduces the experiment. The compact monomer spectrum has its peak in the same position as the experiment, 1650 cm^{-1}, but displays too much off-diagonal structure with its cross-peak ridges at ω_1=1676 and 1630 cm^{-1}. These off-diagonal features are not present in the extended B-chain monomer spectrum, but this spectrum is too diagonally elongated compared to the experiment. Inspection of the NRPS shows a feature at 1630 cm^{-1}, which appears in both monomer spectra, but is more intense for compact monomers. This feature arises from remaining strong vibrational couplings between the B-chain terminus and the helices in the monomer.

3.7 Bright State Analysis of the Calculated Spectra

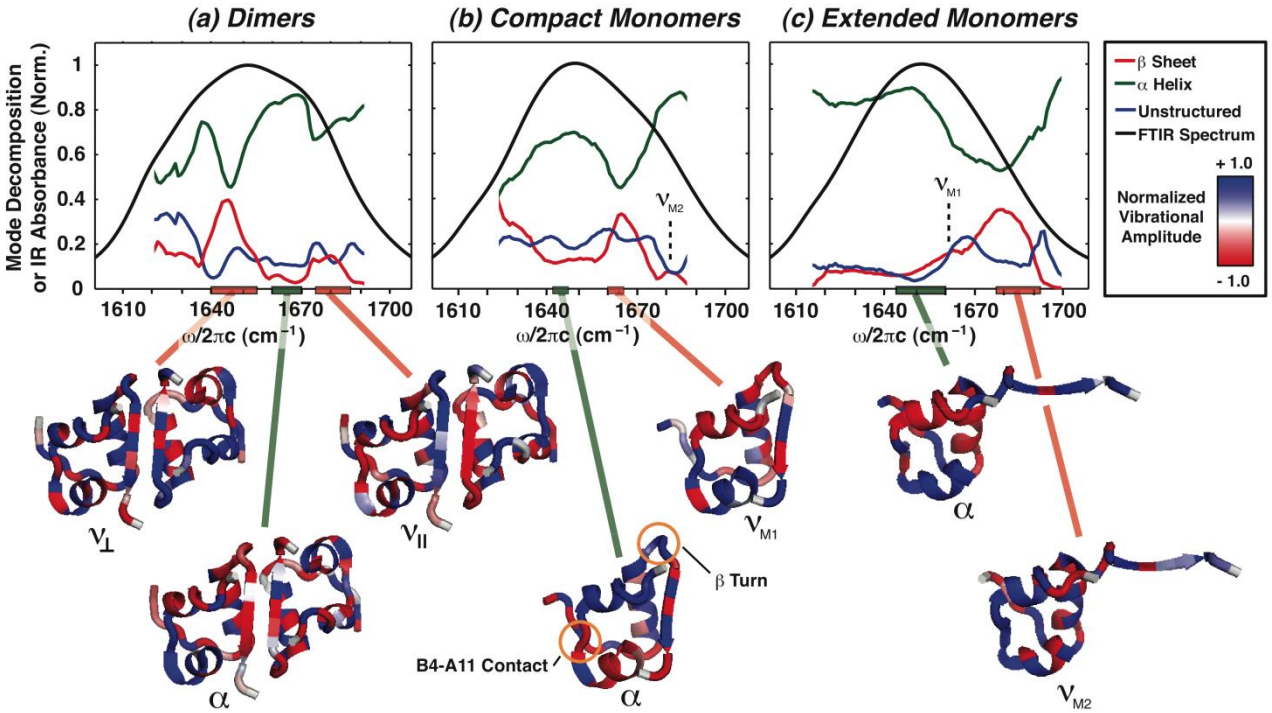

Fig. 7 (Top) Plot of the mode composition from bright state analysis decomposed by secondary structure, and the calculated IR absorption spectrum for the (a) dimer, (b) compact monomer, and (c) extended monomer ensembles. For the mode decomposition, the independent axis gives the beginning of the 5 cm^{-1} window. (Below) Visualizations of the bright states for representative spectral regions, prepared using PyMol.[82] The color (red or blue) represents the vibrational phase of backbone amide I oscillators, while the intensity of color reflects the amplitude of vibration. For each bright state, the vibrational amplitudes were normalized to the large magnitude value.

A quantitative structural assignment of the vibrational modes contributing to different regions of the IR spectrum was performed with doorway mode analysis. This procedure obtains the amide I bright states that carry the IR transition dipole intensity within a given spectral window, provides a visualization of the structures that contribute within that window, and allows the contributions to be decomposed by different secondary structures. Doorway-mode analysis was performed on a 5 cm^{-1} sliding window across the dimer spectrum (Fig. 7a). The mode decomposition was obtained from the bright states within a spectral window by summing over the squared vibrational amplitudes for oscillators within the motif of interest as,

$$P_{s\ se.\ \overline{\nu c}} = \sum_{i}^{s} \sum^{se.\ tc.} |a_i|^2 \qquad \text{Eq. 6}$$

where a_i is the vibrational amplitude of the *i*th oscillator in the unit-normalized bright state. The β-sheet features were found to peak at 1646 cm^{-1} and 1680 cm^{-1} and it was found that the bright states corresponding to these bands display $\nu_{\perp}$ and $\nu_{||}$ symmetry character. These modes are observed in proteins, and here it was noted that they can also arise from intermolecular couplings. Further, the α-helical and β-sheet modes are significantly mixed; each mode appears to be delocalized over the dimer. While the dimer does not rigorously contain a C_2 axis, the α-helix oscillations on each monomer unit are still generally out-of-phase with respect to each other. The direct coupling between α-helices is weak (≤2 cm^{-1}), and the dominant coupling mechanism was found to be through mutual interaction with the β-sheet oscillators.

By comparing the bright states in the two monomer ensembles, the effects of extending the B-strand on the mode structure can be understood. Two representative structures from the monomer ensembles were chosen for the doorway mode analysis. In the calculated 2D IR spectra of the monomers, it was noted that there was intensity at ~1630 cm^{-1} that did not appear in the experimental monomer spectrum. Bright state analysis in this region (not pictured) reveals that this intensity arises from two regions; a hydrogen bond contact between the two main chains (B4 and A11) and, more dominantly, the β turn bridging the B-chain helix and C-terminal strand. Both of these regions are disordered in the ensemble with the extended B-chain strand, and this intensity is reduced.

Comparing the high frequency β-sheet regions for the two monomers, two features appear at 1663 cm^{-1} (ν_{M1}) and 1682 cm^{-1} (ν_{M2}), shown in Fig. 7b and 7c, respectively. The ν_{M1} mode is more intense in the compact monomer, and is a combination of α-helix modes strongly mixed with vibrations on the β strand. The ν_{M2} mode is more intense and broader in the extended B-strand monomer, and is localized to the turn with decreasing participation further along the strand. In summary, these results show that adding disorder to the monomer structure and extending the B-chain strand leads to a loss in the ~1630 cm^{-1} region and localizes the $\nu_{||}$ mode to the turn region, which causes it to blueshifts and broaden.

4 Discussion

4.1 Monomer and dimer spectral signatures across the various IR spectra

There are features common among all of the amide I monomer and dimer spectra that can be interpreted using the structure-based calculations. In all of the IR spectra, a loss is seen at ~1630 cm^{-1} upon dimer dissociation. Using the bright state corresponding to this mode in the insulin dimer, it can be assigned to delocalized mode that is dominated by $\nu_{\perp}$-symmetry vibrations on the two-stranded, anti-parallel β sheet. In the 2D IR spectra, loss of this peak on the diagonal is accompanied by the loss of corresponding cross-peaks to the 1690 cm^{-1} β-sheet and the 1665 cm^{-1} α-helix modes.

The simulations can be used to assign intensity in the 1690 cm^{-1} region. There is partial intensity loss in this region upon dimer dissociation, which is evidenced by diagonal narrowing of the monomer 2D IR spectra and the loss of discrete diagonal and cross peaks in the NRPS. However, a cross-peak ridge at ω_1=1690 cm^{-1} remains in the monomer spectra and diagonal slices of the absorptive 2D IR spectra show a peak intensity ratio ($\nu_{\perp}$ β-sheet : α-helix : $\nu_{\parallel}$ β-sheet) of 6:10:5 in the dimer and 1:10:4 in the monomer. This mode cannot result from dimer contamination, since the dimer signature $\nu_{\perp}$ mode carries a much larger transition dipole than the $\nu_{\parallel}$ mode. The simulations can be used to assign the 1690 cm^{-1} region in both of the monomer spectra as a high frequency β-strand mode. This mode includes contributions from the turn region and is delocalized along the β strand, with less delocalization when the strand is more disordered.

In both the experimental 2D IR and FTIR spectra, a red shift in the peak of the spectrum is seen as the equilibrium is shifted from dimers towards monomers (7 and 9 cm^{-1} for the 2D IR absorptive and NRPS spectra in Fig. 2, and 5 cm^{-1} in the FTIR spectra). In principle, this peak shift may be caused by any of three effects: a change in the coupling to the oscillators in the α-helices, an intrinsic change to the frequencies of the α-helix oscillators, and interference, such as the loss (or gain) of a nearby peak arising from uncoupled modes at higher (or lower) frequency. Each of these effects can be tested using the simulated spectra.

By comparing the calculated spectra of the dimer and the compact monomer, it is found that the α-helix-localized modes are coupled to β-sheet-localized modes; loss of the anti-parallel β sheet leads to an 11 cm^{-1} red shift in the α-helix peak, despite the fact that the α helices in the compact monomer strongly resemble those in the dimer. This coupling was quantified by transforming to a basis of α-helix-localized and $\nu_{\perp}$ β-sheet-localized modes using peak positions from the spectra, and a coupling of 15 cm^{-1} was extracted. The same assumptions applied to the experimental spectra yield a coupling of 9 cm^{-1}. While this comparison provides evidence that the loss of $\nu_{\perp}$ β-sheet modes can shift the α-helix modes, it does not exclude the other mechanisms.

Evidence for a shift in the α-helix peak due to interference can be seen by comparing the two monomer simulations, in which the extension of B chain is accompanied by a 20 cm^{-1} blueshift to the $\nu_{\parallel}$ band, which would additionally contribute to a blueshift in the α-helix peak. An analysis of the frequencies of individual amide I oscillators shows no appreciable frequency shift for the α-helices in any of the calculations. Thus, comparison to the simulations has concluded that the α-helix peak shifts in the monomer spectrum relative to the dimer due to loss of coupling to the $\nu_{\perp}$ mode and perhaps also due to interference with the shifting $\nu_{\parallel}$ mode.

Our analysis showed that the differences between monomer spectra obtained from concentration-dependence and temperature-dependence were negligible. Any changes must be smaller than thermally induced changes to the properties of water and vibrational dynamics of amide I oscillators. These results are consistent with the results of a calorimetry study, which concluded that the insulin dissociation and monomer unfolding transitions are inseparable[75], and our analysis did not require a third thermodynamic species.

While many monomer features were reproduced in the spectra calculated from the NMR structures, neither one entirely reproduced the combination of diagonal elongation and cross-peak ridges evident in the experimental monomer spectrum. To more quantitatively model the monomer spectrum, one might consider a sum of the compact and extended monomer spectra or a weighted sum of the spectra comprising each ensemble. However, when comparing the simulations and experiments, one should note that the theory to calculate amide I protein spectra is still under development. Typically, a set of simulated spectra can used to derive trends that may be compared to the experiment. Direct comparisons of relative amplitudes, frequency splittings, and linewidths is still at a qualitative or semi-quantitative level. With these limitations, one needs to carefully isolate the features that are robust against the many approximations in these calculations, such as the MD force field, mapping snapshots from the simulation to site energies and couplings, and assuming that the dynamics are near the static limit.

4.2 Solvent and temperature effects

The effects of adding ethanol to the thermal dissociation curves can be interpreted by noting its drastic influence on the surface tension of water. While there are many contributions to the free energy for insulin dimer dissociation, there will be a component that is proportional to the hydrophobic surface area and the surface tension. For large solutes (radius > 2 H-bond lengths), this solvation free energy is dominated by enthalpic contributions[76]. It is found that the changes in surface tension upon ethanol addition are consistent with the overall trend in ΔH^0 (see Supplementary Information, Fig. 9), which is a steep decrease from 0-20%, followed by a continuing gradual decrease; the 42% drop in surface tension upon adding 20% volume fraction of ethanol corresponds to a 44% drop in ΔH^0 from 135 to 76 kcal/mol. The concomitant changes in ΔG at 22°C are relatively much smaller, 5.4 kcal/mol to 2.9 kcal/mol, which is a demonstration of the enthalpy-entropy compensation widely seen in protein biophysics.

An estimation of the hydrophobic surface area from the molecular dynamics simulations used to calculate the 2D IR spectra reveals a value of 32 nm^2 for the dimer and a range from 20-25 nm^2 for the monomer, depending on the ensemble chosen. Using an empirical, linear correlation for the hydration enthalpy of hydrocarbons (data obtained from Ref

77)), the 8-18 nm^2 of buried surface area in the dimer corresponds to $\Delta H_{Hydrophobic} \approx$ -22 to -49 kcal/mol in pure water for the hydrophobic contribution to the enthalpy. Such a large hydrophobic stabilization of the dimer rationalizes the experimentally observed change upon adding 20% ethanol, $\Delta\Delta H^0$ = -59 kcal/mol (see Supplementary Information, Fig. 11). These facts are also consistent with an inspection of the structure (**Fig. 1**), all of which indicate that the insulin dimer is largely stabilized by hydrophobic interactions.

Our measured value of K_D from 2D IR experiments, 70 μM for bovine insulin in 0.27 M DCl in D_2O, is consistent with previous measurements in protonated water and similar conditions, which range from 25 μM to 261 μM (literature K_D values are tabulated in the supplementary information). It has been observed that the addition of ethanol greatly destabilizes dimers relative to monomers.[72,20] This work demonstrates that K_D is increased by ~100x, but no corroborating evidence was seen for the previously observed complete dissociation in 5% ethanol.

Our values for the enthalpy and entropy of dimer dissociation are consistent with previous findings in protonated solvents at room temperature. Investigations using uv-vis absorption at pH 2.0, 25˚C, and 0.1 M ionic strength have found ΔH=-17.2 kcal/mol, ΔS=-29 cal/deg mol[19] and ΔH=-12 kcal/mol ΔS=-18 cal/deg mol,[25] which can be compared to our values of -9.6 kcal/mol and -50 cal/deg mol. Differences in these values may be due to our higher ionic strength, lower pH, and deuterated water. Another difference is that our data was sampled at 2.5 °C, which is finer than some previous work (~10 °C), and may have neccessitated $\Delta C_P > 0$ when fitting our data. A more recent calorimetry investigation by Dzwolak et al.[78] was analyzed with attention towards cooperativity in the unfolding, and found a transition temperature (not directly comparable to T_M) around 60 °C. However, our value of ΔC_P is much larger (5 kcal/mol vs 0.5 kcal/mol). Dzwolak et al. also found that D_2O lowered the temperature for aggregation by 7 °C, which provides evidence that straightforward comparisons of melting behavior in protonated and deuterated solvents are not possible.

5 Conclusions

The dimer dissociation reaction of insulin has been probed with two-dimensional infrared spectroscopy and related nonlinear spectroscopies. These techniques provide a structurally sensitive probe of the monomer-dimer transition that were used to measure the binding constant, K_D, and to parameterize a thermodynamic model for the dimer fraction as a function of temperature and concentration for a range of solvent conditions. The monomer-stabilization effect of 20% ethanol was quantified- at 22 °C, it shifts K_D from 210 μM to 6.9 mM- and rationalized by the increased hydrophobic surface area when the dimer interface is exposed.

Atomistic interpretation of the diagonal and off-diagonal spectral changes were provided by comparison to spectra calculated from atomistic molecular dynamics simulations of insulin, which included the effects of structural disorder and spectral interference. This provided both a point of comparison and a complement to NMR and x-ray crytallography structural models. Upon dimer dissociation, the 1630 cm^{-1} $\nu_\perp$ mode was lost, the 1665 cm^{-1} α-helix mode was redshifted, and the 1690 cm^{-1} $\nu_\parallel$ mode decreased in intensity. It was shown that the most sensitive marker for insulin dimers, the $\nu_\perp$ mode, derives its sensitivity due to delocalization over both monomer units mediated by the intermolecular anti-parallel β-sheet. Both spectral interference effects and a loss of coupling to the $\nu_\perp$ mode cause the shift in the α-helix mode. The $\nu_\parallel$ mode undergoes a change in character, from a delocalized β-sheet mode in the dimer to a turn-localized mode that is sensitive to the conformation and disorder in the B-chain C terminus.

From a comparison of the simulated and experimental spectra, it was found that neither structural model entirely reproduces the 2D IR spectrum of the monomer; the experimental monomer spectra show more disorder than the compact monomer model, but less than the extended monomer model. Disorder has been identified as a key variable to describe the monomer ensemble, which suggests that the fly-casting dimerization mechanism should be given further consideration.

One key feature of 2D IR is its intrinsically ultrafast time resolution, which is dictated by the dephasing dynamics of the system and typically extends to a few ps for protein amide modes. While time-resolved techniques are widely applied to study protein folding, they are less commonly used to study the conformational dynamics of protein-protein binding. The combination of time and structural resolution has allowed 2D IR to be used as a transient probe in time-resolved experiments on protein and peptide conformational dynamics and folding, and it will be further exploited to study the monomer/dimer features identified in this investigation. We hope that the background work presented here provides the basis for using insulin dimerization to be studied as a model system for coupled folding/binding protein-protein interactions by a variety of complementary approaches.

Acknowledgements

This work was supported by the National Science Foundation (CHE-0616575 and CHE-0911107). We would also like to thank Benjamin Dietzek for valuable discussions and assistance with data acquisition in the early stages of the experiments.

Notes and references

[a] *Department of Chemistry, Massachusetts Institute of Technology, 77 Massachusetts Avenue, Cambridge, MA 02139 USA. Fax: +1 617 2537030; Tel: +1 617 2534503; E-mail: tokmakof@mit.edu*

† Electronic Supplementary Information (ESI) available: expanded methods, dissociation /melting curves and thermodynamic parameters for all solvent conditions, and a table of K_D values. See DOI: 10.1039/b000000x/

‡ This article was submitted as part of a Themed Issue on Biomolecular Structures: From Isolated Molecules to Living Cells.

1. Baker, E.; Blundell, T.; Cutfield, J.; Cutfield, S.; Dodson, E.; Dodson, G.; Hodgkin, D.; Hubbard, R.; Isaacs, N.; Reynolds, C.; Sakabe, K.; Sakabe, N.; Vijayan, N. *Phil. Trans. R. Soc. B* 1988, **319**, 369.

2. Weiss, M. A.; Nguyen, D.; Khait, I.; Inouye, K.; Frank, B.; Beckage, M.; Oshea, E.; Shoelson, S.; Karplus, M.; Neuringer, L. *Biochemistry* 1989, **28**, 9855-9873.
3. Hua, Q.-X.; Kochoyan, M.; Weiss, M. A. *Proc. Natl. Acad. Sci. USA* 1992, 89, 2379-2383.
4. Keller, D.; Clausen, R.; Josefsen, K.; Led, J. J. *Biochemistry* 2001, **40**, 10732-10740.
5. Zoete, V.; Meuwly, M.; Karplus, M. *J. Mol. Biol.* 2004, **342**, 913-929.
6. Budi, A.; Legge, S.; Treutlein, H.; Yarovsky, I. *Eur. Biophys. J.* 2004, **33**, 121-129.
7. Bocian, W.; Sitkowski, J.; Bednarek, E.; Tarnowska, A.; Kawecki, R.; Kozerski, L. *J. Biomol. NMR* 2008, **40**, 55-64.
8. Hua, Q.-x.; Weiss, M. A. *J. Biol. Chem.* 2004, **279**, 21449-21460.
9. Hua, Q. X.; Gozani, S. N.; Chance, R. E.; Hoffmann, J. A.; Frank, B. H.; Weiss, M. A. *Nat. Struct. Biol.* 1995, **2**, 129-138.
10. Janin, J. *Proteins: Struct. Funct. Bioinf.* 1997, **28**, 153-161.
11. Gabb, H. A.; Jackson, R. M.; Sternberg, M. J. *J. Mol. Biol.* 1997, **272**, 106-120.
12. Shoemaker, B. A.; Portman, J. J.; Wolynes, P. G. *Proc. Natl. Acad. Sci. USA* 2000, **97**, 8868-8873.
13. Creeth, J. *Biochem. J.* 1953, **53**, 41-47.
14. Jeffrey, P. D.; Coates, J. *Biochemistry* 1966, **5**, 3820-3824.
15. Pekar, A.; Frank, B. *Biochemistry* 1972, **11**, 4013-4016.
16. Yu, C.; Chin, C.; Franses, E.; Wang, N. *J. Colloid Interface Sci.* 2006, **299**, 733-739.
17. Koren, R.; Hammes, G. G. *Biochemistry* 1976, **15**, 1165-1171.
18. Nettleton, E. J.; Tito, P.; Sunde, M.; Bouchard, M.; Dobson, C. M.; Robinson, C. V. *Biophys. J.* 2000, **79**, 1053-1065.
19. Lord, R. S.; Gubensek, F.; Rupley, J. A. *Biochemistry* 1973, **12**, 4385-4392.
20. Grudzielanek, S.; Jansen, R.; Winter, R. *J. Mol. Biol.* 2005, **351**, 879-894.
21. Grudzielanek, S.; Jansen, R.; Winter, R. *J. Mol. Biol.* 2005, **351**, 879-894.
22. Bocian, W.; Sitkowski, J.; Tarnowska, A.; Bednarek, E.; Kawęcki, R.; Koźmiński, W.; Kozerski, L. *Proteins: Struct. Funct. Bioinf.* 2008, **71**, 1057-1065.
23. Hassiepen, U.; Federwisch, M.; Mülders, T.; Lenz, V. J.; Gattner, H. G.; Krüger, P.; Wollmer, A. *Eur. J. Biochem.* 1998, **255**, 580-587.
24. Pocker, Y.; Biswas, S. B. *Biochemistry* 1980, **19**, 5043-5049.
25. Strazza, S.; Hunter, R.; Walker, E.; Darnall, D. W. *Arch. Biochem. Biophys.* 1985, **238**, 30-42.
26. Dzwolak, W.; Ravindra, R.; Lendermann, J.; Winter, R. *Biochemistry* 2003, **42**, 11347-11355.
27. Bouchard, M.; Zurdo, J.; Nettleton, E. J.; Dobson, C. M.; Robinson, C. V. *Protein Sci.* 2000, **9**, 1670-1967.
28. Smith, G.; Pangborn, W.; Blessing, R. *Acta Crystallogr., Sect. D: Biol. Crystallogr.* 2003, **59**, 474-482.
29. Derewenda, U.; Derewenda, Z.; Dodson, E. J.; Dodson, G. G.; Reynolds, C. D.; Smith, G. D.; Sparks, C.; Swenson, D. *Nature* 1989, **338**, 594-596.
30. Roy, M.; Brader, M. L.; Lee, R. W.; Kaarsholm, N. C.; Hansen, J. F.; Dunn, M. F. *J. Biol. Chem.* 1989, **264**, 19081-19085.
31. Chang, X.; Jorgensen, A. M.; Bardrum, P.; Led, J. J. *Biochemistry* 1997, **36**, 9409-9422.
32. Hua, Q.; Weiss, M. A. *Biochemistry* 1990, **29**, 10545-10555.
33. Jørgensen, A.; Kristensen, S.; Led, J.; Balschmidt, P. *J. Mol. Biol.* 1992, **227**, 1146-1163.
34. Ludvigsen, S.; Roy, M.; Thøgersen, H.; Kaarsholm, N. C. *Biochemistry* 1994, **33**, 7998-8006.
35. Hua, Q. X.; Hu, S. Q.; Frank, B. H.; Jia, W.; Chu, Y. C.; Wang, S. H.; Burke, G. T.; Katsoyannis, P. G.; Weiss, M. A. *J. Mol. Biol.* 1996, **264**, 390-403.
36. Cheatum, C.; Tokmakoff, A.; Knoester, J. *J. Chem. Phys.* 2004, **120**, 8201-8215.
37. Ganim, Z.; Tokmakoff, A. *Biophys. J.* 2006, **91**, 2636-2646.
38. Zhuang, W.; Hayashi, T.; Mukamel, S. *Angew. Chem. Int. Ed.* 2009, **48**, 3750-3781.
39. Jansen, T. l. C.; Knoester, J. *Acc. Chem. Res.* 2009, **42**, 1405-1411.
40. Jeon, J.; Yang, S.; Choi, J.-H.; Cho, M. *Acc. Chem. Res.* 2009, **42**, 1280-1289.
41. Manor, J.; Mukherjee, P.; Lin, Y.-S.; Leonov, H.; Skinner, J. L.; Zanni, M. T.; Arkin, I. T. *Structure* 2010, **17**, 247-254.
42. Chung, H. S.; Ganim, Z.; Jones, K. C.; Tokmakoff, A. *Proc. Natl. Acad. Sci. USA* 2007, **104**, 14237-14242.
43. Wang, J.; Zhuang, W.; Mukamel, S.; Hochstrasser, R. *J. Phys. Chem. B* 2008, **112**, 5930-5937.
44. Cho, M. *Bull. Korean Chem. Soc.* 2006, **27**, 1940-1960.
45. Hamm, P.; Helbing, J.; Bredenbeck, J. *Annu. Rev. Phys. Chem.* 2008, **59**, 291-317.
46. Ganim, Z.; Chung, H. S.; Smith, A. W.; Deflores, L. P.; Jones, K. C.; Tokmakoff, A. *Acc. Chem. Res.* 2008, **41**, 432-441.
47. Khalil, M.; Demirdöven, N.; Tokmakoff, A. *J. Phys. Chem. A* 2003, **107**, 5258-5279.
48. Jones, K. C.; Ganim, Z.; Tokmakoff, A. *J. Phys. Chem. A*, 2009, **113**, 14060-14066.
49. Lindahl, E.; Hess, B.; van der Spoel, D. *J. Mol. Mod.* 2001, **7**, 306-317.
50. Berendesen, H. J. C.; van der Spoel, D.; van Drunen, R. *Comp. Phys. Comm.* 1995, **91**, 43-56.
51. Essman, U.; Perela, L.; Berkowitz, L.; Darden, H. L.; Pedersen, L. G. *J. Chem. Phys.* 1995, **103**, 8577-8592.
52. Miyamoto, S.; Kollman, P. A. *J. Comp. Chem.* 1992, **13**, 952-962.
53. Berendsen, H. J. C.; Postma, J. P. M.; van Gunsteren, W. F.; Dinola, A.; Haak, J. R. *J. Chem. Phys.* 1984, **81**, 3684-1690.
54. Hess, B.; Bekker, H.; Berendsen, H. J. C.; Fraaije, J. G. E. M. *J. Comp. Chem.* 1997, **18**, 1463-1472.
55. Eisenhaber, F.; Lijnzaad, P.; Argos, P.; Sander, C.; Scharf, M. *J. Comp. Chem.* 1995, **16**, 273-284.
56. Jorgensen, W. L.; Maxwell, D. S.; Tirado-Rives, J. *J. Am. Chem. Soc.* 1996, **118**, 11225-11236.
57. Jorgensen, W. L.; McDonald, N. A. 1998, **424**, 145-155.
58. Jorgensen, W. L.; McDonald, N. A. *J. Phys. Chem. B* 1998, **102**, 8049-8059.
59. Rizzo, R. C.; Jorgensen, W. L. *J. Am. Chem. Soc.* 1999, **121**, 4827-4836.
60. Price, M. L.; Ostrovsky, D.; Jorgensen, W. L. *J. Comp. Chem.* 2001, **22**, 1340-1352.
61. Watkins, E. K.; Jorgensen, W. L. *J. Phys. Chem. A* 2001, **105**, 4118-4125.
62. Kaminski, G. A.; Friesner, R. A.; Tirado-Rives, J.; Jorgensen, W. L. *J. Phys. Chem. B* 2001, **105**, 6474.
63. Eisenberg, D.; McLachlan, A. D. *Nature* 1986, **319**, 199-203.
64. Berendsen, H. J. C.; Grigera, J. R.; Straatsma, T. P. *J. Phys. Chem.* 1987, **91**, 6269-6271.
65. Jansen, T. l. C.; Dijkstra, A. G.; Watson, T. M.; Hirst, J. D.; Knoester, J. *J. Chem. Phys.* 2006, **125**, 044312.
66. Jansen, T. l. C.; Ruszel, W. M. *J. Chem. Phys.* 2008, **128**, 214501.
67. Auer, B. M.; Skinner, J. L. *J. Chem. Phys.* 2007, **127**, 104105.

68. Bour, P.; Keiderling, T. *J. Chem. Phys.* 2003, **119**, 11253-11262.
69. Chung, H. S.; Tokmakoff, A. *J. Phys. Chem. B* 2006, **110**, 2888-2898.
70. Torii, H.; Tasumi, M. *J. Chem. Phys.* 1992, **97**, 86-91.
71. Torii, H.; Tasumi, M. *J. Chem. Phys.* 1992, **97**, 92-98.
72. Dzwolak, W.; Grudzielanek, S.; Smirnovas, V.; Ravindra, R.; Nicolini, C.; Jansen, R.; Loksztejn, A.; Porowski, S.; Winter, R. *Biochemistry* 2005, **44**, 8948–8958.
73. Becktel, W. J.; Schellman, J. A. *Biopolymers* 1987, **26**, 1859-1877.
74. Hua, Q.-x.; Weiss, M. A. *Biochemistry* 1991, **30**, 5505-5515.
75. Huus, K.; Havelund, S.; Olsen, H. B.; van de Weert, M.; Frokjaer, S. *Biochemistry* 2005, **44**, 11171-11177.
76. Southall, N. T.; Dill, K. A.; Haymet, A. D. J. *J. Phys. Chem. B* 2002, **106**, 521-533.
77. Gallicchio, E.; Kubo, M. M.; Levy, R. M. *J. Phys. Chem. B* 2000, **104**, 6271-6285.
78. Dzwolak, W.; Ravindra, R.; Lendermann, J.; Winter, R. *Biochemistry* 2003, **43**, 11347-11355.
79. Timasheff, S. N.; Aune, K. C.; Goldsmith, L. C. *Biochemistry* 1971, **10**, 1617-1622.
80. Yu, Y. B. *J. Pharm. Sci.* 2001, **90**, 2099-2102.
81. Humphrey, W.; Dalke, A.; Schulten, K. *J. Molec. Graphics* 1996, **14**, 33-38.
82. DeLano, W. L. The PyMOL Molecular Graphics System (2002), DeLano Scientific, Palo Alto, CA, USA., http://www.pymol.org.
83. Persistence of Vision Pty. Ltd. (2004), Persistence of Vision Raytracer (Version 3.6), Retrieved from http://www.povray.org/download/.
84. Jørgensen, A.; Kristensen, S.; Led, J.; Balschmidt, P. *J. Mol. Biol.* 1992, **227**, 1146-1163.
85. Kim, Y. S.; Hochstrasser, R. M. *J. Phys. Chem. B* 2009, **113**, 8231-8251.